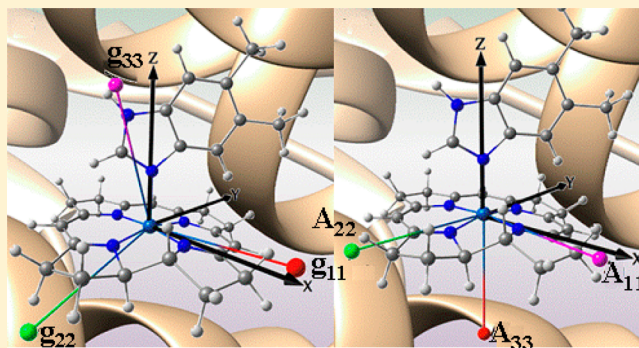


Cob(II)alamin: Relativistic DFT Analysis of the EPR Parameters

Taye B. Demissie,^{†,‡} Michal Repisky,[†] Hui Liu,[§] Kenneth Ruud,[†] and Pawel M. Kozlowski^{*,§}[†]Centre for Theoretical and Computational Chemistry, Department of Chemistry, UiT The Arctic University of Norway, 9037 Tromsø, Norway[‡]Institute of Physical Chemistry, Polish Academy of Sciences, Kasprzaka 44/52, 01-224 Warsaw, Poland[§]Department of Chemistry, University of Louisville, 2320 South Brook Street, Louisville, Kentucky 40292, United States

S Supporting Information

ABSTRACT: Relativistic density functional theory (DFT) has been applied to explore electron paramagnetic resonance (EPR) parameters as well as ground-state spin properties of cob(II)alamin. Cob(II)alamin is an intermediate which participates in many reactions catalyzed by derivatives of vitamin B₁₂ and that can be detected by EPR spectroscopy due to the presence of the paramagnetic Co^{II}(d⁷) center. The full structure of cob(II)alamin and its truncated analogues were examined. Three different DFT functionals, B3LYP, BP86, and PBE, have been applied to obtain the *g*- and *A*-tensors. Both tensors are axially symmetric and can provide useful insight into specific axial ligand interactions. Of the functionals tested, the hybrid B3LYP functional, was found to overestimate the axial bond length, whereas the GGA-type functionals, BP86 and PBE, produced geometries consistent with experimental data. The reliability of nonrelativistic and approximate relativistic methods for the calculation of EPR parameters has also been tested against a fully relativistic four-component approach. Since the EPR parameters are very sensitive to the local environment surrounding Co^{II}, a theoretical (DFT-BP86) estimate of the dependence of the *g*- and *A*-tensors on the metal-to-axial ligand interatomic distance can be directly correlated with EPR measurements. The usefulness of such an approach has been demonstrated for the methionine synthase enzyme where the reduction of cob(II)alamin takes place during the reactivation cycle.



1. INTRODUCTION

Whereas cobalt in B₁₂-dependent enzymatic reactions can exist in +3, +2, or +1 oxidation states,^{1–7} only Co^{II}(3d⁷) is paramagnetic and can be detected by electron paramagnetic resonance (EPR) spectroscopy.⁸ Co^{II} forms the center of cob(II)alamin (Figure 1) where it is ligated by four nitrogens of the corrin macrocycle as well as by dimethylbenzimidazole (DBI) as an axial base which, depending on specific conditions, can be replaced by histidine or water. The EPR spectrum of cob(II)alamin is typical of a low-spin d⁷-cobalt complex and has been the subject of numerous experimental investigations.^{9–18} The hyperfine splitting arises from the interaction of the unpaired electron spin with the magnetic moment of the cobalt-59 nucleus *i.e.*, $I(^{59}\text{Co}) = 7/2$. As expected from the nuclear spin of 7/2, there are eight hyperfine lines; nevertheless the intensity of the highest field hyperfine line is so weak that it is typically not observed. Moreover, additional superhyperfine splittings are observed because of the DBI nitrogen, *i.e.*, $I(^{14}\text{N}) = 1$, coordinated at the lower axial position (Figure 1). In contrast, there is no noticeably resolved hyperfine splitting due to the four in-plane pyrrole nitrogen atoms. Due to the crystal field effect, in the octahedral point group the $d_{x^2-y^2}$ orbital¹⁹ has the highest energy because of the strong equatorial field of the

corrin ligand. Seven electrons in a low-spin configuration thus leave the unpaired electron in the d_{z^2} orbital, which has little overall overlap with the equatorial donor orbitals. As a result, the *g*-tensor is axially symmetric with experimental values $g_{\perp} = 2.24$ and $g_{\parallel} = 2.014$.²⁰ The strong peak at low field corresponds to the g_{\perp} band and shows no resolved hyperfine lines, whereas the center of the g_{\parallel} manifold of bands exhibits hyperfine splitting, and the experimental hyperfine coupling constants are $A(^{59}\text{Co}) = 108$ G and $A(^{14}\text{N}) = 17.5$ G.²⁰

Due to the paramagnetic nature of the Co^{II} ion and the ability to acquire paramagnetic data under biological conditions where concentrations are often very low, EPR spectroscopy has received considerable attention in B₁₂ chemistry. The formation of cob(II)alamin and its interaction with substrate radicals has been extensively studied in adenosylcobalamin (AdoCbl)-dependent enzymes.²¹ Since the *g*-tensor is axially symmetric, the EPR technique can be a very sensitive probe of the local environment surrounding Co^{II} and can provide unique insight into specific axial ligand interactions. Thus, EPR was utilized in the methylcobalamin (MeCbl)-dependent methyltransferases

Received: August 30, 2013

Published: March 31, 2014

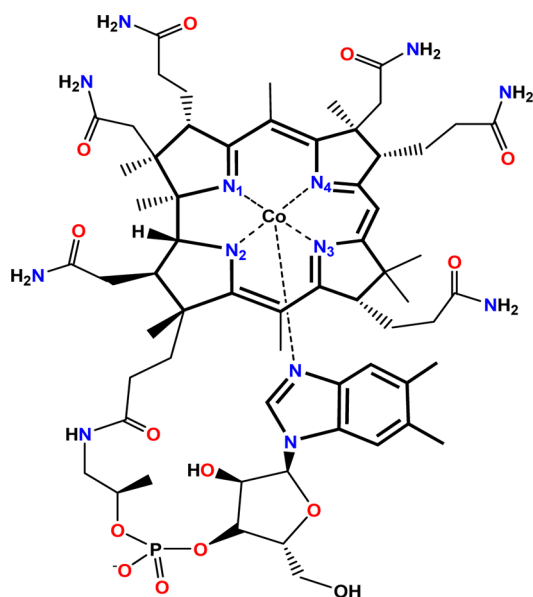


Figure 1. Molecular structure of cob(II)alamin and the truncated structural model abbreviated as $L\text{-}[\text{Co}^{\text{II}}(\text{corrin})]^+$ shown as bold at the center of cob(II)alamin. The axial base (L) on the α -face can be dimethylbenzimidazole (DBI), imidazole (Im), or water (H_2O).

where the enzyme undergoes a reductive reactivation, in which Co^{II} is reduced to Co^{I} with an electron supplied by flavodoxin.²² Likewise in ATP: corrinoid adenosyltransferases such as CobA, PduO, and EutT, the mechanism of Co^{II} reduction, and the synthesis of AdoCbl, has been investigated using EPR spectroscopy.²³

Despite its potential, the major applications of EPR spectroscopy rely on qualitative, rather than quantitative, interpretations of B_{12} -dependent EPR spectroscopic data. Whereas simple models can be used to provide qualitative insight into the ground-state properties and EPR parameters of these systems, recent theoretical studies of open-shell paramagnetic NMR parameters at the relativistic level of theory question the validity of such simple, nonrelativistically derived analyses.²⁴ In particular, their sensitivity with respect to specific local environments have not been explored yet. Because of the sensitive couplings of different EPR parameters observed when analyzing experimental spectra in terms of electron spin-Hamiltonian parameters, extraction of information from the experimental spectra is not straightforward. Hence, accurate EPR parameters of B_{12} are of great importance in order to better understand how the electronic structure of different B_{12} complexes is reflected in the ground-state spin properties. The ability of density functional theory (DFT) to predict EPR parameters can thus potentially facilitate the interpretation of experimental EPR spectra.

EPR parameters are in their nature relativistic, and even the leading-order corrections to the free-electron g value involve the relativistic spin-orbit interaction. Two- and four-component relativistic DFT approaches thus provide the most convenient and natural framework for calculating EPR properties of medium-sized molecules involving even first-row transition metals. However, the number of two- and four-component relativistic studies of EPR parameters of systems of the B_{12} size is very limited. Although perturbation theory approaches have proven to be useful for molecules involving light elements,^{25–29} the recent implementation of EPR

parameters at the two-component^{30–38} and even at the fully relativistic four-component DFT level^{39–44} provides the most reliable framework to calculate the EPR parameters of the cobalt-containing B_{12} complexes. For additional information and further references to relativistic approaches predicting EPR parameters, the reader is referred to a recent review article.⁴⁵

The purpose of the present theoretical study is to perform a systematic analysis of the spin ground-state properties and EPR parameters of cob(II)alamin (Figure 1), which is one of the most common intermediates in B_{12} enzymatic catalysis. In particular, focus will be given to the following issues: (i) What kind of exchange-correlation functionals, *i.e.*, hybrid or GGA-type, is most appropriate to provide reliable estimates for the structure and EPR properties of cob(II)alamin and allow for a direct comparison with experimental data? (ii) Can truncated models for cob(II)alamin be used to calculate EPR parameters? (iii) At what level do relativistic effects have to be treated in the calculations? (iv) How will the replacement of the DBI base by another axial ligand, such as imidazole (Im) or water, tune the EPR parameters of cob(II)alamin? and (v) How can the EPR parameters be correlated with the distance between Co^{II} and the axial ligands? The ultimate goal of this study is to provide new insight into the interpretation of EPR spectroscopic data and how this can be correlated with the specific local structure close to the Co^{II} ion and to provide information on the level of theory required, both in terms of computational model as well as the treatment of relativistic effects, that allows for a reliable analysis of the experimental and theoretical data.

2. COMPUTATIONAL DETAILS

Three cob(II)alamin models (Figure 1) were used to calculate the spin ground-state properties and EPR parameters: (i) the full cob(II)alamin complex based on an available X-ray structure⁴⁶ as well as the optimized cob(II)alamin structural model obtained from the high-resolution crystal structure of the MeCbl cofactor⁴⁷ generated by removing the upper methyl group, (ii) its simplified version *i.e.*, DBI- $[\text{Co}^{\text{II}}(\text{corrin})]^+$, where all the corrin side chains as well as the nucleotide loop have been replaced by hydrogen atoms (Figure 1), (iii) simplified $L\text{-}[\text{Co}^{\text{II}}(\text{corrin})]^+$ models where the lower DBI axial base is replaced by imidazole (Im) or water. (Note that $L\text{-}[\text{Co}^{\text{II}}(\text{corrin})]^+$ follows the notation used in our previous studies.⁴⁸) The geometry optimizations have been performed using the Becke 1988 exchange together with the Perdew 1986 correlation DFT functional (BP86)^{49,50} and the three-parameter Becke with Lee–Yang–Parr exchange-correlation functional (B3LYP),^{51–53} in both cases using the TZ2P⁵⁴ basis set as implemented in the 2012 version of the Amsterdam Density Functional (ADF) program package.⁵⁵ Relativistic corrections were included in the geometry optimization step using the scalar-relativistic zeroth-order-regular-approximation Hamiltonian (SC-ZORA),⁵⁶ as implemented in ADF. Tight convergence criteria were used for the optimization of $L\text{-}[\text{Co}^{\text{II}}(\text{corrin})]^+$, whereas a more relaxed convergence threshold was required in the case of cob(II)alamin due to its molecular size. Frequencies were calculated for the optimized structures of $L\text{-}[\text{Co}^{\text{II}}(\text{corrin})]^+$ and $[\text{Co}^{\text{II}}(\text{corrin})]^+$ to confirm the absence of imaginary frequencies to ensure that the optimized geometry corresponds to a minimum. The Cartesian coordinates of the optimized structures are collected in the Supporting Information. Additionally, the potential energy surface (PES) of the ligand switching model was calculated nonrelativistically

at the BP86/6-31g(d) level of theory using the Gaussian 09 program.⁵⁷

In all reported calculations, the low-spin doublet state ($S = 1/2$) was assumed. Three functionals, B3LYP, BP86 and the Perdew–Burke–Ernzerhof (PBE),⁵⁸ together with the TZ2P basis set, were used to obtain EPR parameters. Relativistic effects were for the EPR parameters accounted for using both scalar (SC-ZORA) and spin–orbit (SO-ZORA) ZORA Hamiltonians, as implemented in ADF, and for comparison, all-electron four-component EPR calculations were also performed, as implemented in the relativistic spectroscopy DFT program ReSpect (version 3.2.0).⁵⁹ In order to facilitate the convergence of the calculations, the augmented Roothaan–Hall Direct Inversion Iterative Subspace (ADIIS)⁶⁰ scheme was used in ADF. The nonrelativistic EPR calculations were also carried out in ADF (NR(a)) and ORCA⁶¹ (NR(b)) programs, and all NR(b) results are listed in the Supporting Information. In both the calculations with ReSpect as well as with the ORCA programs, the BP86 and PBE exchange–correlation (XC) functionals were used together with the uncontracted pcJ-2⁶² basis (upcJ-2) on the light elements and the uncontracted cc-pVTZ⁶³ basis set (ucc-pVTZ) on the cobalt atom. In all geometry optimizations and EPR parameter calculations, spin-unrestricted wave functions were used. The spin densities of the complexes were calculated in ADF and visualized using Chemcraft⁶⁴ with a contour value of 0.008 au.

3. RESULTS AND DISCUSSION

3.1. The Accuracy of Theoretical EPR Parameters As Compared to Experiment: Cob(II)alamin. We focused our initial attention on the cob(II)alamin complex (Figure 1) which can be directly compared to available experimental data. Two different experiments were taken into consideration in order to validate the relativistic DFT calculations: an older single-crystal EPR study of the ¹⁷O-enriched dioxygen adduct of the reduced form of vitamin B₁₂ reported by Jöerin et al.,¹² and a newer study where the hyperfine and nuclear quadrupole parameters were determined using X- and Q-band hyperfine sublevel correlation (HYSCORE) measurements by Harmer et al.¹⁵ As already noted, the EPR spectrum of the corrin-containing Co^{II} exhibits hyperfine structures that suggests a strong coupling between the unpaired electron and the ⁵⁹Co nucleus with $I = 7/2$. The hyperfine coupling constant of cobalt implies that the majority of the unpaired spin density is localized on the cobalt center, increasing the isotropic contribution to the hyperfine coupling constants of cobalt. As expected, the corresponding unpaired spin density is located on the cobalt and is partially delocalized to the nitrogen atom of the axial DBI ligand (Figure 2). The spin-density profile on Co^{II} resembles the shape of the d_z^2 orbital. There is also noticeable spin density on the ligated DBI nitrogen atom, thereby increasing the corresponding hyperfine coupling constant of the axial ligand nitrogen atom (Figure 2).

Considering that the EPR parameters are very sensitive to the local environment surrounding Co^{II}, we first consider the molecular geometry, as it is important that the calculated geometry closely matches that of the experimental X-ray data.⁴⁶ The popular hybrid functional B3LYP has been shown to not perform well and give axial bond distances that are too long.^{46,65} For instance in cob(II)alamin, the Co^{II}–N(axial) distance calculated by B3LYP is ~0.1 Å too long compared to the experimental value of 2.13 Å.⁴⁶ An attempt to optimize the structure of the cob(II)alamin complex (Figure 1) using B3LYP

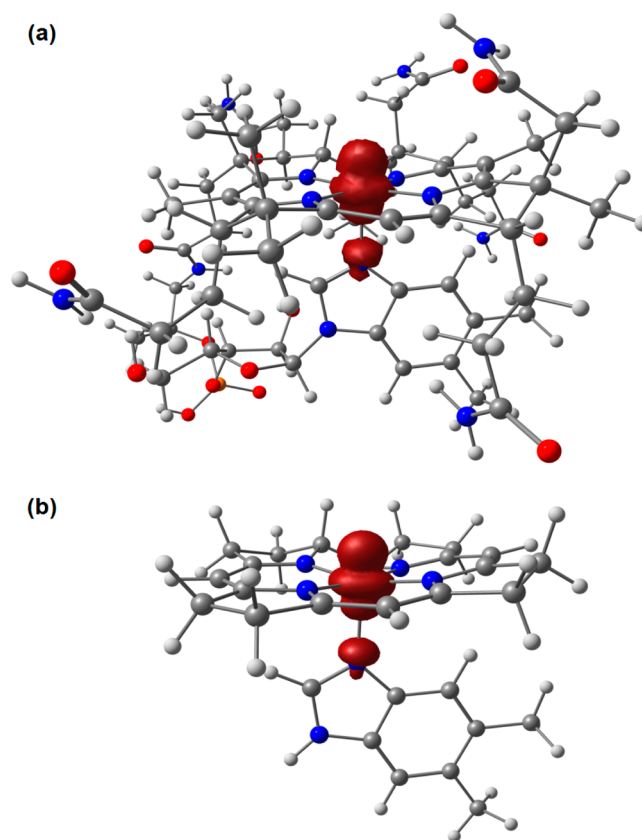


Figure 2. Spin density profiles corresponding to cob(II)alamin (a) and DBI-[Co^{II}(corrin)]⁺ (b). Coarse grid for cob(II)alamin and medium grid for DBI-[Co^{II}(corrin)]⁺ were used to plot the spin densities using BP86/TZ2P.

turned out to be problematic because the optimization lead to a too large Co^{II}–N(DBI) axial bond distance. Converged B3LYP geometries could however be obtained for the truncated L-[Co^{II}(corrin)]⁺ models (*vide infra*). In contrast, the geometry optimization performed using the BP86 functional converged well for the cob(II)alamin complex, the optimized bond length of Co^{II}–N(DBI) (2.159 Å) matching almost perfectly the experimental bond length of 2.13 Å.⁴⁶ Excellent agreement with experimental observations for the axial bonding has also been observed for other cob(II)alamins using GGA-type functionals, such as BP86 and PBE.⁶⁶ The BP86/TZ2P optimized geometry of cob(II)alamin was for this reason used in all calculations on the full cob(II)alamin complex.

The calculated EPR parameters are summarized in Table 1. Three different functionals, B3LYP, BP86, and PBE, have been applied to calculate the g - and A -tensors, in all cases using the BP86/TZ2P optimized geometry. Let us first consider the results for the g -tensor. Regardless of applied functional, the calculated g -tensor components are consistent with an axial spin system (*i.e.*, $g_{33} \equiv g_{\parallel}$, $g_{22} \leq g_{11} \equiv g_{\perp}$). These results are in agreement with the experimental data and also consistent with the spin density plot in which the spin is located on the metal d_z^2 orbital as shown in Figure 2. g_{33} is in the direction of the z -axis of the molecule which is normal to the plane of the corrin ring, but the BP86/TZ2P calculation shows that it is tilted by 16.8°, whereas g_{11} and g_{22} are oriented along the Co^{II}–N(corrin) bonds with a slight shift to the carbon atom next to the nitrogen atoms of the ring. All functionals underestimate the experimental data, the extent being dependent on the

Table 1. Comparison of Computed *g*-Tensor and *A*-Tensor (in MHz) Values of Cob(II)alamin with Experimental Data for the Structure Optimized Using BP86 Functional^h

	NR			SC-ZORA			SO-ZORA			exp. ^a	exp. ^b
	B3LYP	BP86	PBE	B3LYP	BP86	PBE	B3LYP	BP86	PBE		
<i>g</i> ₁₁	-	-	-	-	-	-	2.1876	2.1433	2.1464	2.272	2.310 ± 0.005
<i>g</i> ₂₂	-	-	-	-	-	-	2.1478	2.1146	2.1167	2.230	2.190 ± 0.005
<i>g</i> ₃₃	-	-	-	-	-	-	2.0069	2.0014	2.0012	2.004	2.004 ± 0.005
<i>g</i> _{iso} ^e	-	-	-	-	-	-	2.1141	2.0864	2.0881	2.169	2.168 ± 0.005
⁵⁹ Co											
<i>A</i> ₁₁	-97.53	-53.63	-58.75	-41.17	-44.10	-49.75	53.23	53.65	50.17	30	65 ± 12
<i>A</i> ₂₂	-33.06	-16.63	12.07	27.30	25.58	20.50	84.57	92.13	88.64	40	80 ± 12
<i>A</i> ₃₃	443.34	450.60	447.09	445.24	457.29	453.22	429.18	447.34	443.25	305	302 ± 10
<i>A</i> _{iso} ^e	104.25	137.87	133.47	143.79	146.26	141.33	188.99	197.71	194.02	125	149 ± 11.3 ^g
¹⁴ N ^c											
<i>A</i> ₁₁	41.07	52.60	52.81	41.08	52.48	52.70	44.56	52.26	52.45	-	45 ± 2
<i>A</i> ₂₂	42.06	53.64	53.80	42.07	53.53	53.69	45.88	53.38	53.52	-	45 ± 2
<i>A</i> ₃₃	49.98	65.35	65.48	50.00	65.17	65.32	55.18	65.29	65.41	-	53 ± 2
<i>A</i> _{iso} ^e	44.37	57.20	57.36	44.37	57.06	57.24	48.54	56.98	57.13	50	48 ± 2
¹⁴ N ^d											
<i>A</i> ₁₁	1.23	2.00	2.05	1.23	2.00	2.05	1.89	2.02	2.07	1.75	-
<i>A</i> ₂₂	1.56	2.40	2.43	1.57	2.40	2.44	2.48	2.47	2.52	1.75	-
<i>A</i> ₃₃	1.97	2.99	3.03	1.98	3.00	3.03	2.62	3.00	3.04	2.10	-
<i>A</i> _{iso} ^e	1.59	2.46	2.50	1.60	2.47	2.51	2.33	2.50	2.54	1.87 ^f	-

^aExperimental data from Harmer *et al.*¹⁵ ^bExperimental data from Jöerin *et al.*¹² ^cCorresponds to the nitrogen atom of DBI axially coordinated to Co^{II}. ^dCorresponds to the remote nitrogen atom of DBI. ^eComputed as $X_{\text{iso}} = (X_{11} + X_{22} + X_{33})/3$. ^fSimilar experimental value of $A_{\text{iso}} = 1.85$ was reported by Ke *et al.*¹³ ^gCalculated statistically from the experimental values. ^hThe geometry of cob(II)alamin corresponds to BP86/TZ2P optimized structure where Co^{II}-N(DBI) = 2.159 Å. The NR, SC-ZORA and SO-ZORA results were obtained using ADF.

applied functional. It appears that B3LYP performs slightly better for the *g*₁₁ and *g*₂₂ components, but for *g*₃₃ other functionals give values closer to experimental data. However, as will be shown later, based on the comparison of the results obtained for the SO-ZORA approximation compared to the full mDKS results obtained for Co^{II}(corrin)⁺ and the corresponding water complex (*vide infra*), we can expect that the SO-ZORA approach underestimates the *g*-tensor components, and thus better agreement with experiment can be expected at the full four-component relativistic level of theory.

The *A*-tensor components reported in Table 1 show the pattern of axial EPR-active species ($A_{11} \leq A_{22} \equiv A_{\perp}$ and $A_{33} \equiv A_{\parallel}$), in agreement with the experimental findings.^{12,15} The *A*-tensor of cobalt suggests a strong dipole–dipole interaction between the cobalt nucleus and the unpaired electron in the *d*_{z²} orbital. Relativistic effects are found to be very important for the in-plane components of the ⁵⁹Co hyperfine coupling constants, with large changes being observed both going from the purely nonrelativistic hyperfine coupling constants to the scalar relativistic ZORA approximation, with only the SO-ZORA approximation giving results in qualitative agreement with experiment. The importance of SO corrections in the calculation of heavy-element hyperfine coupling constants has been noted also in smaller systems.^{67,68} Nevertheless, also at the SO-ZORA level of theory, the components of the cobalt hyperfine tensors are for all functionals overestimated, in particular for the component perpendicular to the plane, for which all functionals predict *A*₃₃ to be too large compared to experiment by about 140 MHz. In general, the differences in the calculated hyperfine couplings obtained with the different functionals are small compared to the deviation from experiment. As we will return to in Section 3.3, the cobalt hyperfine couplings are very sensitive to the description of relativistic effects, and the differences observed compared to

experiment may be due to limitations in the SO-ZORA approximation.

As mentioned above, the unpaired electron spin density is partially delocalized to the axial ligand, increasing the hyperfine coupling constant of the DBI nitrogen atom. The results for the DBI nitrogen atom directly attached to the cobalt atom obtained from the B3LYP functional and SO Hamiltonian are *A*₁₁ = 44.5, *A*₂₂ = 45.9, and *A*₃₃ = 55.2 MHz which are in better agreement with the experimental results of 45 ± 2, 45 ± 2, and 53 ± 2, respectively,¹² than the GGA results. Even though the agreement with experiment is fairly good, the BP86 and PBE functionals overestimate these tensors by 7 to 10 MHz compared to results obtained with the B3LYP functional. However, it must be kept in mind that the B3LYP functional is not appropriate for describing the axial bond, resulting in a significant overestimation of the Co^{II}-N(DBI) bond length. Both scalar and spin–orbit relativistic effects are important, the former being the most important of the two. The *A*-tensor components of the nitrogen atom of DBI most distant from the corrin ring show the interaction of this nitrogen with the unpaired electron largely located on the cobalt atom. The calculated values of all the *A*-tensor components of the remote DBI nitrogen atom (*A*₁₁ = 2.00, *A*₂₂ = 2.40, and *A*₃₃ = 3.00 MHz, using the BP86 functional) are in good agreement with the experimental results (1.75, 1.75, and 2.10 MHz, respectively).¹⁵ The results for the corrin ring nitrogen atoms listed in Table 1 are also in fair agreement with the experimental results reported by Harmer *et al.*¹⁵

Overall, the calculated results show that the EPR parameters of the full cob(II)alamin structure can be directly compared to the experimental results with a reasonable degree of confidence, even though the calculations are expensive for large molecular systems of this kind. Our results show that relativistic corrections as well as correct geometries are essential in

Table 2. Calculated *g*-Tensor and *A*-Tensor (in MHz) Values of DBI-[Co^{II}(corrin)]⁺ for the Structure Optimized using B3LYP Functional^c

	NR			SO-ZORA			mDKS	
	B3LYP	BP86	PBE	B3LYP	BP86	PBE	BP86	PBE
<i>g</i> ₁₁	-	-	-	2.2096	2.1463	2.1496	2.1540	2.1574
<i>g</i> ₂₂	-	-	-	2.1825	2.1277	2.1305	2.1333	2.1362
<i>g</i> ₃₃	-	-	-	2.0054	2.0026	2.0024	2.0029	2.0025
<i>g</i> _{iso} ⁵⁹ Co	-	-	-	2.1325	2.0922	2.0942	2.0967	2.0987
<i>A</i> ₁₁	-55.27	-8.41	-15.01	105.57	106.54	101.30	87.97	80.30
<i>A</i> ₂₂	-9.58	41.32	35.11	131.58	143.69	138.48	138.62	130.47
<i>A</i> ₃₃	474.72	490.28	485.57	463.39	492.29	486.28	493.02	482.27
<i>A</i> _{iso} ¹⁴ N ^a	136.62	174.40	168.56	233.51	247.51	242.02	239.87	231.01
<i>A</i> ₁₁	38.27	49.79	50.01	37.95	49.21	49.42	46.97	46.89
<i>A</i> ₂₂	39.13	50.74	50.91	38.85	50.22	50.38	48.12	47.97
<i>A</i> ₃₃	46.77	62.15	62.31	46.65	61.80	61.95	60.05	59.91
<i>A</i> _{iso} ¹⁴ N ^b	41.39	54.23	54.41	41.15	53.75	53.92	51.71	51.59
<i>A</i> ₁₁	1.43	2.39	2.46	1.44	2.42	2.48	2.17	2.25
<i>A</i> ₂₂	1.72	2.75	2.81	1.76	2.82	2.88	2.59	2.65
<i>A</i> ₃₃	2.09	3.28	3.34	2.08	3.29	3.35	3.06	3.11
<i>A</i> _{iso}	1.75	2.81	2.87	1.76	2.84	2.90	2.61	2.67

^aCorresponds to the nitrogen atom of DBI axially coordinated to Co^{II}. ^bCorresponds to the remote nitrogen atom of DBI. ^cThe geometry corresponds to the B3LYP/TZ2P optimized structure where Co^{II}-N(DBI) = 2.284 Å. The NR and SO-ZORA results were obtained using ADF program, whereas the four-component mDKS results using the ReSpect program.

Table 3. Calculated *A*-Tensor (in MHz) and *g*-Tensor Values of DBI-[Co^{II}(corrin)]⁺ for the Structure Optimized Using BP86 Functional^c

	NR			SO-ZORA			mDKS	
	B3LYP	BP86	PBE	B3LYP	BP86	PBE	BP86	PBE
<i>g</i> ₁₁	-	-	-	2.1856	2.1271	2.1295	2.1324	2.1340
<i>g</i> ₂₂	-	-	-	2.1636	2.1126	2.1146	2.1191	2.1195
<i>g</i> ₃₃	-	-	-	2.0052	2.0015	2.0014	2.0013	2.0017
<i>g</i> _{iso} ⁵⁹ Co	-	-	-	2.1181	2.0804	2.0818	2.0843	2.0851
<i>A</i> ₁₁	-101.33	-58.42	-63.42	41.89	41.47	37.31	21.14	22.72
<i>A</i> ₂₂	-50.06	-5.54	-10.25	76.80	84.52	80.44	69.51	64.67
<i>A</i> ₃₃	439.03	446.64	443.27	428.58	448.87	444.43	447.64	432.28
<i>A</i> _{iso} ¹⁴ N ^a	95.88	127.56	123.20	182.43	191.62	187.40	179.43	173.22
<i>A</i> ₁₁	43.91	55.76	55.98	43.52	55.13	55.34	52.96	52.73
<i>A</i> ₂₂	44.97	56.86	57.02	44.60	56.28	56.44	54.18	53.92
<i>A</i> ₃₃	53.34	69.13	69.27	53.12	68.72	68.86	67.11	66.81
<i>A</i> _{iso} ¹⁴ N ^b	47.41	60.58	60.75	47.08	60.04	60.22	58.09	57.82
<i>A</i> ₁₁	1.72	2.76	2.84	1.72	2.79	2.86	2.58	2.64
<i>A</i> ₂₂	2.07	3.18	3.25	2.11	3.26	3.33	3.09	3.14
<i>A</i> ₃₃	2.46	3.74	3.81	2.46	3.75	3.81	3.57	3.61
<i>A</i> _{iso}	2.08	3.23	3.30	2.10	3.27	3.33	3.08	3.13

^aCorresponds to the nitrogen atom of DBI axially coordinated to Co^{II}. ^bCorresponds to the remote nitrogen atom of DBI. ^cThe geometry corresponds to BP86/TZ2P optimized structure where Co^{II}-N(DBI) = 2.184 Å. The NR and SO-ZORA results were obtained using ADF program, whereas the four-component mDKS results using the ReSpect program.

order to provide qualitatively correct results. The results are, however, very sensitive to the geometry chosen, the description of the local environment, as well as the treatment of relativistic corrections (in addition to the choice of exchange-correlation functional), and we will now explore these aspects further by investigating the *g*-tensor and hyperfine coupling tensors in

smaller model systems, benchmarking also our results against full four-component relativistic calculations.

3.2. DBI-[Co^{II}(corrin)]⁺. Having shown that fair agreement with experiment can be obtained using two-component SO-ZORA calculations using hybrid functionals on the full complex (with the exception of *A*₃₃(⁵⁹Co) hyperfine coupling constant), let us now turn to the question of whether truncated models

can be used to study the ground-state properties and EPR parameters of cob(II)alamin. We investigate a truncated model in which the side chains of the MeCbl structure have been removed. We will also explore the reliability of the SO-ZORA approach by comparison against full four-component Dirac-Kohn–Sham.

Let us first consider the importance of the choice of geometry for the EPR parameters themselves. In Table 2, we have collected the EPR parameters calculated with the geometry optimized using the B3LYP functional, whereas those listed in Table 3 use the geometry optimized with the BP86 functional. The B3LYP functional gives a Co–N(DBI) distance of 2.284 Å, whereas the BP86 functional gives 2.184 Å, in both cases longer than the experimentally observed bond distance and the BP86-optimized structure of the full complex. The spin-density profile in Figure 2 shows the localization of the unpaired electron in the cobalt d_{z^2} orbital. As was the case for cob(II)alamin, there is a noticeable spin density on the DBI nitrogen atom attached to the cobalt.

If we first consider the g -tensor components calculated at the BP86-optimized geometry (Table 3), we note that there are only rather small differences in the g -tensor components calculated at the SO-ZORA level compared to those obtained for the full complex, despite the much longer Co–N(DBI) bond distance for the truncated model. It is interesting to note that comparing the truncated and full models for the BP86-optimized structures, only g_{22} shows any noticeable structural dependence in the case of the B3LYP calculations, whereas this sensitivity is only observed in case of g_{11} for the GGAs BP86 and PBE. This observation suggests that there are subtle, but significant, differences in the spin densities calculated using GGA functionals and the hybrid B3LYP functional. Comparing instead the g -tensor components for the truncated model obtained with the B3LYP and BP86-optimized geometries, both in-plane components (g_{11} and g_{22}) change, irrespective of whether B3LYP, BP86, or PBE is used to calculate the g -tensor components. If we compare the g -tensor components calculated using SO-ZORA with the results obtained at the four-component mDKS level of theory, the differences are rather small, the mDKS results in general being somewhat larger than the SO-ZORA results. Overall, the g -tensor components calculated at the SO-ZORA level of theory for the geometry optimized using the B3LYP functional (listed in Table 2) are closer to the experimental results measured for B₁₂, but considering the much too long Co–N(DBI) bond length, this is likely to be accidental.

Comparing the cobalt hyperfine tensor components for the full complex and that of the truncated model optimized at the B3LYP or BP86 levels of theory, we note that whereas the A_{33} component is rather insensitive to the computational level, the in-plane components vary much more significantly. For the BP86-optimized truncated model, A_{11} and A_{22} are about 10% smaller than the components for the full structure, whereas for the B3LYP-optimized truncated model they are about 60–100% larger than those in the BP86-optimized full model, also overshooting the experimental data significantly. For the BP86-optimized truncated model, there are significant differences between the four-component mDKS results and the SO-ZORA results, the latter being almost twice as large as the mDKS results for the A_{11} component. Similar trends in terms of reduced values of the A -tensor components when going to the full four-component level is also observed for the B3LYP-optimized structure.

For the DBI nitrogen atoms, the difference between the results obtained from both geometries are small compared to those of cobalt; the isotropic tensors obtained from the geometry optimized using the BP86 functional are in excellent agreement with the experimental value for the remote DBI nitrogen atom. The A -tensors of these nitrogen atoms are also in good agreement with the spin-density plot shown in Figure 2. The analysis of the g - and A -tensor values for the geometry of the truncated complex optimized without any geometrical constraints and using tight convergence criteria are comparable to those of the full cob(II)alamin structure. These results suggest that the EPR parameters of the full structure can be modeled reasonably well using the truncated model of cob(II)alamin using the BP86-optimized structure.

The g_{33} -tensor and A_{33} (^{59}Co) hyperfine tensor axes do not coincide, both sharing the z axis but pointing in opposite directions. However, A_{11} (^{59}Co) and g_{11} as well as A_{22} (^{59}Co) and g_{22} coincide with the x and y axes, respectively. The orientations of the g -tensor components obtained using the BP86 functional on the BP86-optimized geometry are plotted in Figure 3. The figure shows that g_{33} is normal to the plane of

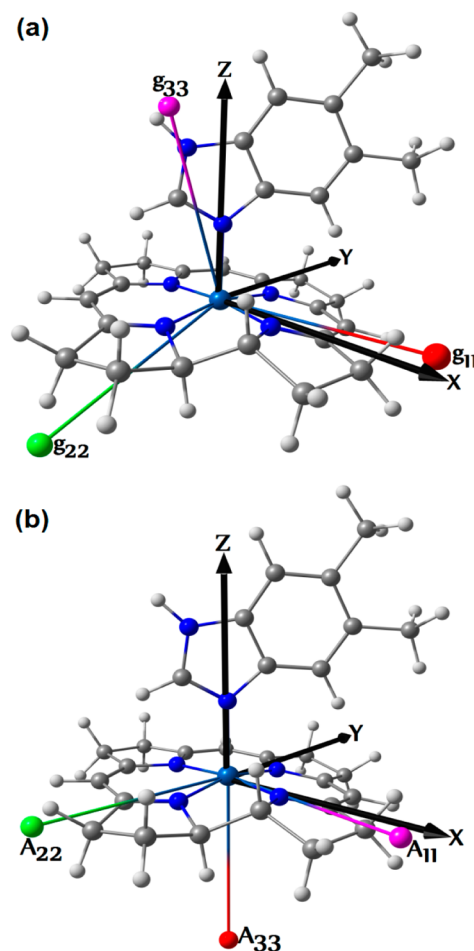


Figure 3. Orientation of g -tensors (a) and $A(^{59}\text{Co})$ -tensors (b) of DBI-[Co^{II}(corrin)]⁺ obtained from SO-ZORA/BP86 and symbolized using dummy atoms. Colors represent the magnitudes of tensors: red = maximum, green = medium, and pink = minimum. g_{11} is lifted out of the corrin plane by 11.5°, whereas g_{22} is below the plane of the ring by 11.9° and both are parallel to the Co^{II}–N(corrin) vectors. g_{33} is tilted by 17.7° from the Co^{II}–N(DBI) vector. The molecular axes systems are shown using black arrows.

Table 4. Calculated A-Tensor (in MHz) and g-Tensor Values of $[\text{Co}^{\text{II}}(\text{corrin})]^+$ and $\text{H}_2\text{O}-[\text{Co}^{\text{II}}(\text{corrin})]^+$ for the Structures Optimized Using BP86 Functional^a

	$[\text{Co}^{\text{II}}(\text{corrin})]^+$					$\text{H}_2\text{O}-[\text{Co}^{\text{II}}(\text{corrin})]^+$					
	SO-ZORA		mDKS		exp. ^a	SO-ZORA		mDKS		exp. ^a	exp. ^b
	BP86	PBE	BP86	PBE		BP86	PBE	BP86	PBE		
g_{11}	2.2964	2.3322	2.3184	2.3363	2.814	2.1623	2.1672	2.1712	2.1760	2.382	2.320
g_{22}	2.2440	2.2608	2.2613	2.2696	2.534	2.1503	2.1544	2.1586	2.1624	2.302	2.320
g_{33}	2.0006	2.1216	1.9877	1.9856	1.935	2.0029	2.0027	2.0008	2.0004	1.992	1.997
g_{iso}^c	2.1803	2.2382	2.1891	2.1972	2.428	2.1052	2.1081	2.1102	2.1129	2.225	2.212
⁵⁹ Co											
A_{11}	802.6	543.8	541.2	530.0	495	533.0	524.5	229.6	213.4	206	213
A_{22}	811.6	800.7	562.1	553.6	556	554.9	546.1	249.3	232.8	229	213
A_{33}	1099.9	811.7	786.1	766.5	695	936.1	924.5	601.6	581.1	392	395
A_{iso}^c	904.7	718.7	629.8	616.7	582	674.6	665.0	360.2	342.4	276	274
¹⁷ O											
A_{11}	-	-	-	-	-	-63.3	-63.1	-54.1	-56.0	-	-
A_{22}	-	-	-	-	-	-63.8	-63.5	-54.5	-56.3	-	-
A_{33}	-	-	-	-	-	-95.9	-95.6	-86.8	-88.3	-	-
A_{iso}^c	-	-	-	-	-	-74.3	-74.1	-65.1	-66.9	-	-

^aExperimental data from Liptak et al.¹⁸ ^bExperimental data from Stich et al.¹⁷ ^cComputed as $X_{\text{iso}} = (X_{11} + X_{22} + X_{33})/3$. ^dThe geometry corresponds to the BP86/TZ2P optimized structure where $\text{Co}^{\text{II}}-\text{O}(\text{H}_2\text{O}) = 2.210 \text{ \AA}$. The two-component SO-ZORA results were obtained using the ADF program, whereas the four-component mDKS results were obtained using the ReSpect program.

the ring, pointing in the opposite direction of A_{33} on cobalt, but tilted by 17.7° from the $\text{Co}^{\text{II}}-\text{N}(\text{DBI})$ vector. The g_{11} and g_{22} are on the $\text{Co}^{\text{II}}-\text{N}(\text{corrin})$ bonds and g_{11} is lifted out of the corrin plane by 11.5° , whereas g_{22} is below the plane by 11.9° . The principal axes of the g-tensors obtained from the geometry optimized using the B3LYP functional deviate by approximately 1° to 2.3° from the corresponding orientations shown in Figure 3.

3.3. $[\text{Co}^{\text{II}}(\text{corrin})]^+$ and $\text{L}-[\text{Co}^{\text{II}}(\text{corrin})]^+$ ($\text{L} = \text{H}_2\text{O}$ or Im).

Let us now turn to an analysis of the structural dependence of the EPR parameters of B_{12} -related complexes by exploring the dependence of the EPR parameters on the coordination number and on the strength of complexation. We do this by exploring the four-coordinated $[\text{Co}^{\text{II}}(\text{corrin})]^+$ complex and the corresponding five-coordinated $\text{L}-[\text{Co}^{\text{II}}(\text{corrin})]^+$ species, using both water and imidazole as axial ligands. From Table 4, we see that the g_{11} - and g_{22} -tensors of the four-coordinated cobalamin complex are greater than those of the five-coordinated complexes. Similarly, all the hyperfine coupling constants of cobalt are larger in the four-coordinated complex than in the five-coordinated ones. This suggests that in $[\text{Co}^{\text{II}}(\text{corrin})]^+$ the majority of the unpaired spin density is localized on the cobalt center but that the unpaired electron spin density in $\text{H}_2\text{O}-[\text{Co}^{\text{II}}(\text{corrin})]^+$ is partially delocalized on the axial ligand and thereby increasing the corresponding hyperfine coupling constant of the axial ligand oxygen atom. The same effects are observed for $\text{Im}-[\text{Co}^{\text{II}}(\text{corrin})]^+$ (see Table S3). However, the interaction of the oxygen atom of the water axial ligand with the unpaired electron is greater compared to that of the nitrogen of the imidazole and DBI ligands. The spin-density plots in Figure S3 also show that for both four- and five-coordinated complexes, the unpaired electron mainly localizes on the cobalt d_{z^2} orbital.

A somewhat surprising observation from the data in Table 4 is the strong dependence of the calculated ^{59}Co hyperfine coupling constant on the description of the relativistic effects in the $\text{H}_2\text{O}-[\text{Co}^{\text{II}}(\text{corrin})]^+$ complex, the four-component relativistic results for the cobalt hyperfine coupling constant being

about half the value of the results obtained with the SO-ZORA results. These differences are significantly larger than for any of the other systems studied and show that the treatment of relativistic effects is critical and that good performance for some systems does not guarantee equally good performance for other systems, even if they are structurally related. The mDKS results for the $\text{H}_2\text{O}-[\text{Co}^{\text{II}}(\text{corrin})]^+$ complex are in very good agreement with experiment. For instance, the experimental results for A_{11} , A_{22} , and A_{33} of ^{59}Co in $[\text{Co}^{\text{II}}(\text{corrin})]^+$ are 495, 556, and 695 MHz, while those of the four-component relativistic calculated values using the PBE functional are 530, 553.6, and 766.5 MHz, respectively. A similar agreement was obtained for $\text{H}_2\text{O}-[\text{Co}^{\text{II}}(\text{corrin})]^+$ for the A-tensor components of the cobalt ion where the experimental results are 206, 229, and 392 MHz and the four-component relativistic calculated values are 213.4, 232.8, and 581.1 MHz using the PBE functional.

Previous studies based on EPR spectroscopic measurements by Liptak et al.²² indicate that the presence of a tyrosine ligand elongates the $\text{Co}^{\text{II}}-\text{OH}_2$ distance. The values of g_{11} , g_{22} , and g_{33} reported in the same paper in the presence of Y1139 are 2.406, 2.320, 1.995, whereas the values of A_{11} , A_{22} , and A_{33} for ^{59}Co are 208, 231, and 387 MHz, respectively, but these results are nevertheless in agreement with those reported for a water-coordinated complex from the same group¹⁸ (2.382, 2.302, and 1.992 for the g-tensor components and 206, 229, and 392 MHz for the $A(^{59}\text{Co})$ -tensor components, respectively). These results indicate that the species analyzed in both studies are five-coordinated complexes in the presence of H_2O as an axial ligand. Experimental results reported by Doorslaer et al.¹⁶ for the g-tensors of the four-coordinated complex in toluene are respectively 2.447, 2.447, and 1.990. On the other hand, the values in methanol are 2.327, 2.327, and 1.999, respectively. The values for the A_{11} , A_{22} , and A_{33} for ^{59}Co reported by Doorslaer et al.¹⁶ in toluene are 273, 273, and 430 MHz, whereas these values in methanol are 217, 217, and 395 MHz, respectively. These experimental results and our calculated

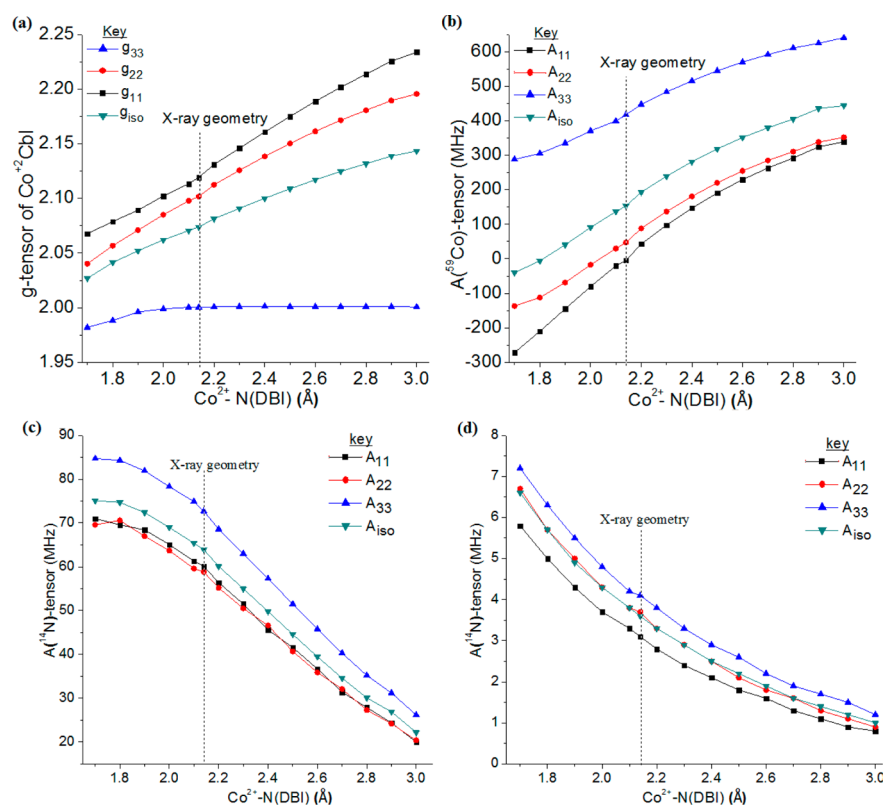


Figure 4. (a) Co^{II}-N(DBI) distance dependence of *g*-tensor components, (b) *A*(⁵⁹Co)-tensor components of DBI-[Co^{II}(corrin)]⁺, (c) Co^{II}-N(DBI) distance dependence of *A*(¹⁴N)-tensor components of the DBI nitrogen atom attached to Co^{II}, (d) *A*(¹⁴N)-tensor components of the remote nitrogen of DBI of DBI-[Co^{II}(corrin)]⁺. Note that all calculations correspond to BP86 functional and SO-ZORA Hamiltonian. The dotted line represents the Co^{II}-N(DBI) distance taken from the X-ray structure by removing the side chains.

values for H₂O-[Co^{II}(corrin)]⁺ obtained from the four-component relativistic method are in reasonable agreement.

3.4. Co^{II}-N(axial) Distance Dependence of DBI-[Co^{II}(corrin)]⁺ and H₂O-[Co^{II}(corrin)]⁺. When the distance between Co^{II} and N(DBI) increases, the metal could lose its interaction with the axial ligand so that the unpaired electron may be completely situated on the cobalt atom. The *g*₁₁ and *g*₂₂ values, those in the plane of the ring, are dependent on the metal-to-ligand separation distance, whereas *g*₃₃, perpendicular to the plane of the ring, is independent of the separation distance and deviates negligibly from the *g*-tensor value of the free electron, 2.0023, see Figure 4. The *g*₁₁ and *g*₂₂ values increase with increasing Co^{II}-N(DBI) distance, suggesting considerable spin-orbit coupling. These results also explain why *g*₁₁ and *g*₂₂ are considerably larger for the four-coordinated complex than those for five- or six-coordinated complexes and show that EPR parameters can be used to determine the coordination state of B₁₂ derivative complexes.

The *A*-tensor values for the cobalt ion are also dependent on the metal-to-ligand separation distance. With an increase in the separation distance, all the *A*-tensor values of the metal increase. This indicates an increased interaction of the unpaired electron with the cobalt nucleus, resulting in a nearly complete localization of the unpaired electron on cobalt at larger distances. At shorter distances, the unpaired electron could also be shared with the ligated nitrogen atom of DBI, decreasing the magnitude of the *A*-tensor of the metal. The study of [Co^{II}(corrin)]⁺ *A*-tensor distance dependence (see Figure 4) indicates that the truncated corrin ring is sufficient for modeling the EPR spectra of the full cob(II)alamin complex. However, as

noted above, an appropriate functional must be employed for optimizing the structure.

The *A*-tensor of the DBI nitrogen atoms versus Co^{II}-N(DBI) distance is plotted in Figure 4. Unlike the cobalt *A*-tensor values, the absolute values of the *A*-tensors of the nitrogen atoms decrease when the metal-to-ligand distance increases, further confirming the reduced interaction of the unpaired electron with the ¹⁴N nucleus. When the DBI ligand is closer to cobalt, the *A*-tensor components of the ligated nitrogen atom increase, confirming that the unpaired electron is also distributed on the ligated DBI nitrogen atom. At larger separation distances, the *A*-tensor components of the nitrogen attached to cobalt decrease by more than 30 MHz from those of the optimized as well as the simplified structure of Co^{II}Cbx. This sensitivity of the *A*-tensor components are of considerable importance for establishing the coordination number of related complexes.

The increase in distance between the cobalt center and the water molecule also affects the *g*-tensor and hyperfine coupling tensor of the H₂O-[Co^{II}(corrin)]⁺ complex as shown in Figure 5, largely displaying the same trends as observed for the imidazole complex. When the water ligand is removed, the singly occupied molecular orbital (SOMO) will localize more on the cobalt atom (see the Supporting Information for details), reflected in the observation that the *A*(⁵⁹Co) values of the five-coordinated complex are less than the values of the four-coordinated complex (see Table 4). Unlike the cobalt, the absolute values of the *A*-tensors of the oxygen atom decrease when the metal-to-ligand distance increases, confirming the

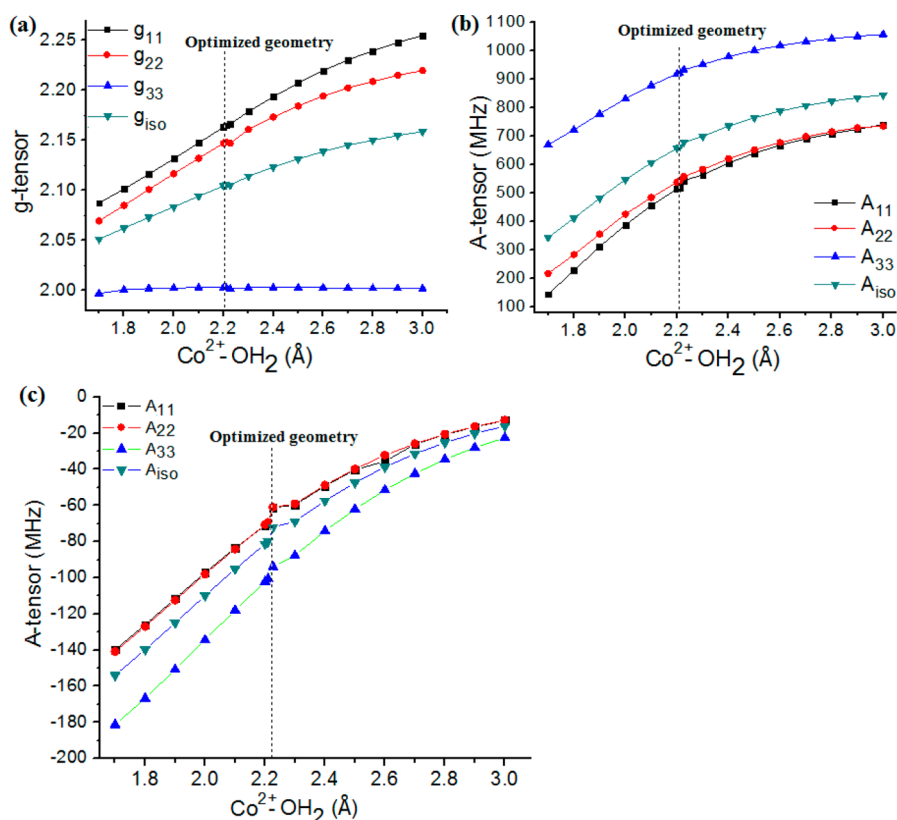


Figure 5. (a) $\text{Co}^{\text{II}}\text{-O}(\text{H}_2\text{O})$ distance dependence of g -tensor components, (b) $A(^{59}\text{Co})$ -tensor components, (c) $\text{Co}^{\text{II}}\text{-O}(\text{H}_2\text{O})$ distance dependence of $A(^{17}\text{O})$ -tensor components of $\text{H}_2\text{O}\text{-}[\text{Co}^{\text{II}}(\text{corrin})]^+$. Note that all the calculations correspond to BP86 functional and SO-ZORA Hamiltonian. The dotted line represents the $\text{Co}^{\text{II}}\text{-O}(\text{H}_2\text{O})$ optimized distance.

decrease in the interaction of the unpaired electron with the ^{17}O nucleus.

3.5. Reactivation Cycle of Methionine Synthase Enzyme: Ligand Displacement and Coordination of Co^{II} Center. Considering the sensitivity of the EPR parameters with respect to specific axial ligand interactions, their values can provide insight into B_{12} -dependent enzymatic reactions, where the specific local environment plays a key role. The usefulness of such an approach can be demonstrated for cobalamin-dependent methionine synthase, which carries out the methyl group transfer from CH_3 -folate to homocysteine (Hcy) forming methionine (Met).⁶⁹ The reaction cycle consists of the main catalytic cycle and the reactivation cycle. During the first half of the catalytic cycle, the methyl group is transferred from the MeCbl cofactor to Hcy, forming Met and enzyme-bound cob(I)alamin. The high reactivity of cob(I)alamin makes it a prime target for sporadic oxidation, resulting in a catalytic incompetent cob(II)alamin form. This deactivation reaction is reported to occur once every 2000 turnover cycles.⁷⁰ In order to maintain the efficient catalytic cycle, the activated MeCbl form must be regenerated by the reductive methylation of cob(II)alamin. It has been suggested^{22,71} that the reactivation cycle involves an axial ligand switch to generate a five-coordinate enzyme-bound cob(II)alamin with the axial H_2O ligand on the “upper” (*i.e.*, β -face) of the corrin (see Figure 6a). The subsequent steps involve a significant lengthening, or even rupture, of the $\text{Co}\text{-OH}_2$ bond of the cofactor, followed by one-electron reduction. Although it was initially suggested that reduction involves four-coordinated Co^{II} ,²² recent theoretical studies predicted formation of a $\text{Co}^{\text{I}}\text{-H}$ bond,⁷² implying that

the reduction should proceed via five-coordinated species.⁷³ Since the axial ligand displacement as well as reduction steps involve Co^{II} , the process can be probed by EPR spectroscopy.²²

In order to explore axial ligand displacements, we first computed the potential energy surface (PES) representing the $\text{Im}\text{-}[\text{Co}^{\text{II}}(\text{corrin})]^+\cdots\text{H}_2\text{O}$ and $\text{Im}\cdots[\text{Co}^{\text{II}}(\text{corrin})]^+\text{-OH}_2$ cases, *i.e.*, the ligand displacement between imidazole and water (Figure 6b and 6c). These model calculations can provide a useful picture regarding the interaction of Co^{II} with the two axial ligands and shed some light on the corresponding enzymatic reaction. As the imidazole departs from the Co^{II} ion, the $\text{Co}^{\text{II}}\text{-OH}_2$ distance decreases and finally water is attached to the Co^{II} ion. As shown in Figure 6, the global minimum is located at $\text{Co}^{\text{II}}\text{-N}(\text{Im}) = 2.15 \text{ \AA}$ and $\text{Co}^{\text{II}}\text{-OH}_2 = 2.50 \text{ \AA}$ (note that in the absence of the second ligand, the optimized distances are 2.12 and 2.20 \AA , respectively.) Interestingly, when the imidazole is displaced and water gets closer to the Co^{II} center, the ligand displacement is an energetically uphill reaction and the PES does not show any corresponding energy minimum. The topology of the PES does not imply that the switch of the ligand should take place but rather suggests that cob(II)alamin species should remain five-coordinated with respect to Im with the water ligand weakly attached. However, one has to keep in mind that the presence of the enzymatic environment can make the interaction between cobalt and water more stable.

To further explore the reaction involving axial ligand displacement, we also computed EPR parameters for selected axial distances corresponding to $\text{Co}^{\text{II}}\text{-N}(\text{Im})$ lengthening and at the same time shortening of the $\text{Co}^{\text{II}}\text{-O}(\text{H}_2\text{O})$ bond (Table S3, Supporting Information). From these calculations, it is

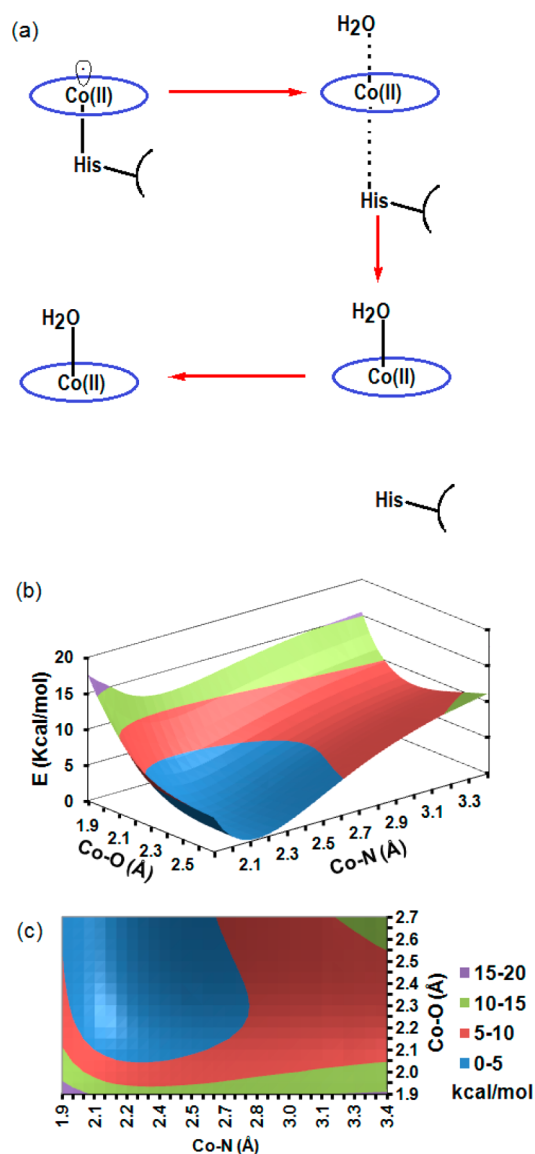


Figure 6. (a) The schematic representation of the ligand switch between the imidazole and water axial ligands and (b) 3D and (c) 2D potential energy surfaces of the ligand switch calculated with BP86/6-31g(d). The global minimum is located at $\text{Co}^{\text{II}}-\text{N}(\text{Im}) = 2.15 \text{ Å}$ and $\text{Co}^{\text{II}}-\text{OH}_2 = 2.50 \text{ Å}$.

apparent that one of the components of the g -tensor, in particular g_{33} being perpendicular to the average plane of the ring, is insensitive to the ligand separation distances. The other two, *i.e.* g_{11} and g_{22} , show some sensitivity, but they cannot be used to provide a specific correlation with distance. On the other hand, components of the A -tensor can be correlated with specific axial distances. Let us recall that the fit parameters from the simulation of the EPR spectra reported in ref 22 for the cobalamin-dependent methionine synthase in the activation conformation are 208, 231, and 387, respectively. These values clearly fit the case where water is close to the Co^{II} center. The A_{33} component is off and is more in line with the $\text{Co}-\text{N}(\text{Im})$ bond actually being shorter. Based on this observation, it is tempting to suggest that a tightening of the axial ligands takes place when water gets closer to the Co^{II} , consistent with the energy minimum pathway shown in Figure 6c. Similar tightening of axial ligands has been observed for the corrinoid

[Fe-S] protein (CoFeSP), where the reduction of the Co^{II} center by the [Fe-S] takes place.⁷⁴

4. SUMMARY AND CONCLUSIONS

Based on detailed computational investigations and comparisons with experimental observations, we are now in a position to answer the five questions raised as motivation for this work. (i) We have shown that the BP86 functional gives structures that for the full cob(II)alamin complex agrees well with X-ray structures, whereas B3LYP fails to converge and for the truncated model systems provides structures that have too long $\text{Co}-\text{N}(\text{DBI})$ bond distance. Once a proper geometry has been obtained, the difference in calculated EPR properties is smaller between B3LYP and BP86, B3LYP giving somewhat better agreement with experiment than BP86. However, this may be fortuitous due to limitations in the computational model (vibrational effects, solvent effects, the treatment of relativistic effects etc.). (ii) We have shown that truncated models provide EPR data that are of a quality that allows for qualitative agreement with experimental observations as well as the results obtained for the full model. Nevertheless, as the truncated models show much longer $\text{Co}-\text{N}(\text{DBI})$ bond lengths than the full model, caution is needed. (iii) We have demonstrated that spin-orbit effects are essential in order to get qualitatively correct results for the hyperfine coupling constants and in particular for the ligand centers. In most cases, SO-ZORA agrees well with the results of four-component mDKS calculations, though the notable exception of the ^{59}Co hyperfine tensor suggests that this conclusion should be used with caution and that four-component calculations are clearly preferable whenever possible, in particular if there are no experimental data to guide the analysis. (iv) and (v) We have shown that the EPR parameters, through their measure of the spin density on the cobalt atom, provide a very stringent test for the coordination number, large in-plane g -tensor and ^{59}Co hyperfine coupling tensors suggested a four-coordinated complex. The g -tensors in the plane of the ring (g_{11} and g_{22}) are dependent on the metal-to-ligand separation, whereas the one perpendicular to the plane of the ring (g_{33}) is independent of the separation distance and deviates negligibly from the g -tensor value of the free electron, 2.0023. We have demonstrated that this observation is due to the fact that the g -tensor and hyperfine coupling tensors are a sensitive measure on the extent of delocalization of the SOMO unpaired electron onto the ligands, an effect promoted by the proximity of the ligand to the metal center.

The g -tensor components in $[\text{Co}^{\text{II}}(\text{corrin})]^+$ and $[\text{C}^{\text{II}}(\text{corrin})]^+$ are approximately axially symmetric for g_{33} (g_{\parallel}) which is perpendicular to the corrin plane, while the other two components almost lie in the plane of the ring. The A -tensor components also show the pattern of axial EPR-active species ($A_{11} \leq A_{22} = A_{\perp}$ and $A_{33} = A_{\parallel}$). The g_{33} - and $A_{33}(^{59}\text{Co})$ hyperfine tensors share the z axis and point in opposite directions. $A_{11}(^{59}\text{Co})$ and g_{11} , as well as $A_{22}(^{59}\text{Co})$ and g_{22} , coincide with the x and y axes, respectively. The unpaired electron spin density is partially delocalized on the axial ligand, leading to an increase in the hyperfine coupling constant of the DBI nitrogen atom attached to the metal center compared to the four corrin nitrogen atoms. The corrin nitrogen atoms that are close to the meso carbon atoms (N_3 and N_4) have A -tensor components of the same category, and those on the opposite side (N_1 and N_2) also have similar behavior, suggesting that the corrin nitrogen atoms belong to two different classes.

■ ASSOCIATED CONTENT

■ Supporting Information

The optimized structures and additional EPR parameters. This material is available free of charge via the Internet at <http://pubs.acs.org>.

■ AUTHOR INFORMATION

Corresponding Author

*E-mail: pawel@louisville.edu.

Notes

The authors declare no competing financial interest.

■ ACKNOWLEDGMENTS

This work has been supported by the Research Council of Norway through a Centre of Excellence grant 179568/V30) and through a research grant (Grant No. 177558/V00), as well as from the Norwegian Program for Supercomputing (NOTUR) through a grant of computer time (nn4654k). T.B.D. has been supported by the International PhD Projects Programme of the Foundation for Polish Science cofinanced with the European Regional Development Fund within Innovative Economy Operational Programme "Grants for Innovation". We also would like to acknowledge the Cardinal Research Cluster (Supercomputing Facilities at the University of Louisville) for providing computational resources in PES calculations.

■ REFERENCES

- (1) Pilbrow, J. R. EPR of B_{12} -Dependent Enzyme Reactions and Related Systems. In *B₁₂ Vol. 1: Chemistry*; Dolphin, D., Ed.; John Wiley & Sons: New York, 1982; pp 449–457.
- (2) Marzilli, L. G. The Two B_{12} Cofactors: Influence of the *trans* Nitrogen Ligand on Homolytic and Heterolytic Processes. In *Bioinorganic Catalysis*, 2nd ed.; Reedijk, J., Bouwman, E., Eds.; Marcel Dekker, Inc.: New York, 1999; pp 423–468.
- (3) *Vitamin B₁₂ and B₁₂ Proteins*; Kräutler, B., Arigoni, D., Golding, B. T., Eds.; Wiley-VCH: New York, 1998.
- (4) Gerfen, G. EPR Spectroscopy of B_{12} -Dependent Enzymes. In *Chemistry and Biochemistry of B₁₂*; Banerjee, R., Ed.; John Wiley & Sons: New York, 1999; pp 165–195.
- (5) Banerjee, R.; Ragsdale, S. W. *Annu. Rev. Biochem.* **2003**, *72*, 209–247.
- (6) Matthews, R. G.; Koutmos, M.; Datta, S. *Curr. Opin. Struct. Biol.* **2008**, *18*, 658–666.
- (7) Randaccio, L.; Geremia, S.; Demitri, N.; Wuerger, J. *Molecules* **2010**, *15*, 3228–3259.
- (8) See, for example Palmer, G. Electron Paramagnetic Resonance of Metalloproteins. In *Physical Methods in Bioinorganic Chemistry*; Que, L., Jr., Ed.; University Science Books: Sausalito, CA, 2000; pp 121–185.
- (9) Hogenkamp, H. P. C.; Barker, H. A.; Mason, H. S. *Arch. Biochem. Biophys.* **1963**, *100*, 353–359.
- (10) Schrauzer, G. N.; Lee, L.-P. *J. Am. Chem. Soc.* **1968**, *90*, 6541–6543.
- (11) Bayston, J. H.; Looney, F. D.; Pilbrow, J. R.; Winfield, M. E. *Biochemistry* **1970**, *9*, 2164–2172.
- (12) Jöerin, E.; Schweiger, A.; Guenthard, H. H. *J. Am. Chem. Soc.* **1983**, *105*, 4277–4286.
- (13) Ke, S.-H.; Torrent, M.; Museav, D. G.; Morokuma, K.; Warncke, K. *Biochemistry* **1999**, *38*, 12681–12689.
- (14) Trommel, J. S.; Warncke, K.; Marzilli, L. *J. Am. Chem. Soc.* **2001**, *123*, 3358–3366.
- (15) Harmer, J.; Van Doorslaer, S.; Gromov, I.; Schweiger, A. *Chem. Phys. Lett.* **2002**, *358*, 8–16.
- (16) Doorslaer, S. V.; Jeschke, G.; Epel, B.; Goldfarb, D.; Eichel, R.-A.; Kräutler, B.; Schweiger, A. *J. Am. Chem. Soc.* **2003**, *125*, 5915–5927.
- (17) Stich, T. A.; Buan, N. R.; Brunold, T. C. *J. Am. Chem. Soc.* **2004**, *126*, 9735–9749.
- (18) Liptak, M. D.; Fleischacker, A. S.; Matthews, R. G.; Telser, J.; Brunold, T. C. *J. Phys. Chem. B* **2009**, *113*, 5245–5254.
- (19) Note that this labeling of the d orbitals of cobalt assumes that the z axis is perpendicular to the corrin macrocycle. Furthermore, the x and y axes that define the x-y plane of the corrin intersect the nitrogen atoms.
- (20) See for example Schrauzer et al. ref 10.
- (21) See for example Pilbrow, J. R. Chapter 12, pp 449–457 in ref 1. Gerfen, G. J. Chapter 6, pp 165–195 in ref 4.
- (22) Liptak, M. D.; Datta, S.; Matthews, R. G.; Brunold, T. C. *J. Am. Chem. Soc.* **2008**, *130*, 16374–16381.
- (23) Park, K.; Mera, P. E.; Escalante-Semerena, J. C.; Brunold, T. C. *Inorg. Chem.* **2012**, *51*, 4482–4494.
- (24) Komorovsky, S.; Repisky, M.; Ruud, K.; Malkina, O. L.; Malkin, V. G. *J. Phys. Chem. A* **2013**, *117*, 14209–14219.
- (25) Schreckenbach, G.; Ziegler, T. *J. Phys. Chem. A* **1997**, *101*, 3388–3399.
- (26) Malkina, O. L.; Vaara, J.; Schimmelpfennig, B.; Munzarova, M.; Malkin, V. G.; Kaupp, M. *J. Am. Chem. Soc.* **2000**, *122*, 9206–9218.
- (27) Neese, F. *J. Chem. Phys.* **2001**, *115*, 11080–11096.
- (28) Rinkevicius, Z.; de Almeida, K. J.; Vahtras, O. *J. Chem. Phys.* **2008**, *129*, 064109.
- (29) Eriksson, L. A.; Malkina, O. L.; Malkin, V. G.; Salahub, D. R. *J. Chem. Phys.* **1994**, *100*, 5066–5075.
- (30) van Lenthe, E.; Wormer, P. E. S.; van der Avoird, A. *J. Chem. Phys.* **1997**, *107*, 2488–2498.
- (31) Neyman, K. M.; Ganyushin, D. I.; Matveev, A. V.; Nasluzov, V. A. *J. Phys. Chem. A* **2002**, *106*, 5022–5030.
- (32) Malkin, I.; Malkina, O. L.; Malkin, V. G.; Kaupp, M. *J. Chem. Phys.* **2005**, *123*, 244103–16.
- (33) Sandhoefer, B.; Neese, F. *J. Chem. Phys.* **2012**, *137*, 094102–15.
- (34) Verma, P.; Autschbach, J. *J. Chem. Theory Comput.* **2013**, *9*, 1052–1067.
- (35) van Lenthe, E.; van der Avoird, A.; Wormer, P. E. S. *J. Chem. Phys.* **1998**, *108*, 4783–4796.
- (36) Neese, F. *J. Chem. Phys.* **2003**, *118*, 3939–3948.
- (37) Malkin, I.; Malkina, O. L.; Malkin, V. G.; Kaupp, M. *Chem. Phys. Lett.* **2004**, *396*, 268–276.
- (38) Verma, P.; Autschbach, J. *J. Chem. Theory Comput.* **2013**, *9*, 1932–1948.
- (39) Case, D. A. *J. Chem. Phys.* **1985**, *83*, 5792.
- (40) Arratia-Perez, R.; Hernandez-Acevedo, L. *J. Chem. Phys.* **1998**, *109*, 3497.
- (41) Arratia-Perez, R.; Hernandez-Acevedo, L. *J. Chem. Phys.* **2003**, *118*, 7425.
- (42) Repisky, M.; Komorovsky, S.; Malkin, E.; Malkina, O. L.; Malkin, V. G. *Chem. Phys. Lett.* **2010**, *488*, 94–97.
- (43) Malkin, E.; Repisky, M.; Komorovsky, S.; Mach, P.; Malkina, O. L.; Malkin, V. G. *J. Chem. Phys.* **2011**, *134*, 044111–8.
- (44) Hrobarik, P.; Repisky, M.; Komorovsky, S.; Hrobarikova, V.; Kaupp, M. *Theor. Chem. Acc.* **2011**, *129*, 715–725.
- (45) Autschbach, J. *J. Chem. Phys.* **2012**, *136*, 150902–15.
- (46) Krautler, B.; Keller, W.; Kratky, C. *J. Am. Chem. Soc.* **1989**, *111*, 8937–8940.
- (47) Randaccio, L.; Furlan, M.; Geremia, S.; Slouf, M.; Srnova, I.; Toffoli, D. *Inorg. Chem.* **2000**, *39*, 3403–3413.
- (48) See for example Kozlowski, P. M.; Zgierski, M. Z. *J. Phys. Chem. B* **2004**, *108*, 14163–14170.
- (49) Becke, A. D. *Phys. Rev. A* **1988**, *38*, 3098–3100.
- (50) Perdew, J. P. *Phys. Rev. B* **1986**, *33*, 8822–8824.
- (51) Becke, A. D. *J. Chem. Phys.* **1993**, *98*, 5648–5652.
- (52) Lee, C.; Yang, W.; Parr, R. G. *Phys. Rev. B* **1988**, *37*, 785–789.
- (53) Stephens, P. J.; Devlin, F. J.; Chabalowski, C. F.; Frisch, M. J. *J. Phys. Chem.* **1994**, *98*, 11623–11627.

- (54) Lenthe, E. v.; Baerends, E. J. *J. Comput. Chem.* **2003**, *24*, 1142–1156.
- (55) *ADF2012, SCM, Theoretical Chemistry*; Vrije Universiteit: Amsterdam, The Netherlands, 2012. <http://www.scm.com/> (accessed April 6, 2014).
- (56) Lenthe, E. v.; Ehlers, A. E.; Baerends, E. J. *J. Chem. Phys.* **1999**, *110*, 8943–8953.
- (57) Frisch, M. J. G.; Trucks, W.; Schlegel, H. B.; Scuseria, G. E.; Robb, M. A.; Cheeseman, J. R.; Scalmani, G.; Barone, V.; Mennucci, B. G.; Petersson, A.; Nakatsuji, H.; Caricato, M.; Li, X.; Hratchian, H. P.; Izmaylov, A. F.; Bloino, J.; Zheng, G.; Sonnenberg, J. L.; Hada, M. E. M.; Toyota, K.; Fukuda, R.; Hasegawa, J.; Ishida, M.; Nakajima, T.; Honda, Y.; Kitao, O.; Nakai, H.; Vreven, T.; Montgomery, J. A.; Peralta, J. E.; Ogliaro, F.; Bearpark, M.; Heyd, J. J.; Brothers, E.; Kudin, K. N.; Staroverov, V. N.; Kobayashi, R.; Normand, J.; Raghavachari, K.; Rendell, A.; Burant, J. C.; Iyengar, S. S.; Tomasi, J.; Cossi, M.; Rega, N.; Millam, J. M.; Klene, M.; Knox, J. E.; Cross, J. B.; Bakken, V.; Adamo, C.; Jaramillo, J.; Gomperts, R.; Stratmann, R. E.; Yazyev, O.; Austin, A. J.; Cammi, R.; Pomelli, C.; Ochterski, J. W.; Martin, R. L.; Morokuma, K.; Zakrzewski, V. G.; Voth, G. A.; Salvador, P.; Dannenberg, J. J.; Dapprich, S.; Daniels, A. D.; Farkas, O.; Foresman, J. B.; Ortiz, J. V.; Cioslowski, J.; Fox, D. J. *Gaussian 09*, Revision A.02; Gaussian, Inc.: Wallingford, CT, 2009.
- (58) Perdew, J. P.; Burke, K.; Ernzerhof, M. *Phys. Rev. Lett.* **1996**, *77*, 3865–3868.
- (59) *ReSpect*, version 3.2.0, 2012; Relativistic Spectroscopy DFT program of authors Repisky, M.; Komorovsky, S.; Malkin, V. G.; Malkina, O. L.; Ruud, K.; Kaupp, M.; with contributions from Arbuznikov, A. V.; Bast, R.; Ekstrom, U.; Malkin, I.; Malkin, E., <http://rel-qchem.sav.sk> (accessed April 6, 2014).
- (60) Hu, X.; Yang, W. *J. Chem. Phys.* **2010**, *132*, 054109.
- (61) *The Orca Program System*, version 2.6; modern electronic structure program package written by Neese, F. et al. 2008. <http://www.thch.uni-bonn.de/tc/orca/> (accessed April 6, 2014).
- (62) Jensen, F. *Theor. Chem. Acc.* **2010**, *126*, 371–382.
- (63) Balabanov, N. B.; Peterson, K. A. *J. Chem. Phys.* **2005**, *123*, 064107.
- (64) Chemcraft. <http://www.chemcraftprog.com/> (accessed April 6, 2014).
- (65) Kuta, J.; Patchkovskii, S.; Zgierski, M. Z.; Kozlowski, P. M. *J. Comput. Chem.* **2006**, *27*, 1429–1437.
- (66) Kuta, J.; Wuerges, J.; Randaccio, L.; Kozlowski, P. M. *J. Phys. Chem. A* **2009**, *113*, 11604–11612.
- (67) Sojka, Z.; Pietrzyk, P. *Spectrochim. Acta, Part A* **2004**, *60*, 1257–1265.
- (68) Malkin, E.; Malkin, I.; Malkina, O. L.; Malkin, V. G.; Kaupp, M. *Phys. Chem. Chem. Phys.* **2006**, *8*, 4079–4085.
- (69) See for example Matthews, R. G.; Koutmos, M.; Datta, S. *Curr. Opin. Struct. Biol.* **2008**, *18*, 658–666.
- (70) Koutmos, M.; Datta, S.; Patridge, K. A.; Smith, J. L.; Matthews, R. G. *Proc. Natl. Acad. Sci. U.S.A.* **2009**, *106*, 18527–18532.
- (71) Drummond, J. T.; Huang, S.; Blumenthal, R. M.; Mathews, R. G. *Biochemistry* **1993**, *32*, 9290–9295.
- (72) Kumar, M.; Kozlowski, P. M. *Angew. Chem., Int. Ed.* **2011**, *50*, 8702–8705.
- (73) Kumar, M.; Kumar, N.; Hirao, H.; Kozlowski, P. M. *Inorg. Chem.* **2012**, *51*, 5533–5538.
- (74) Meister, W.; Henning, S. E.; Jeoung, J.-H.; Lendzian, F.; Dobbek, H.; Hildebrandt, P. *Biochemistry* **2012**, *51*, 7040–7042.